Journal of Marine Science and Technology

Volume 26 | Issue 3 Article 14

USING REPRODUCING KERNEL PARTICLE METHOD FOR SHALLOW WATER PROBLEMS

Chien-Ting Sun
CR Classification Society.

On-Lei Annie Kwok
Department of Civil Engineering, National Taiwan University, Taipei, Taiwan, R.O.C.

Pai-Chen Guan
Department of Systems Engineering and Naval Architecture, National TaiwanOcean University, Keelung, Taiwan, R.O.C Center of Excellence for Ocean Engineering., paichen@ntou.edu.tw

Wen-Kai Shih
Department of Systems Engineering and Naval Architecture, National Taiwan Ocean University, Keelung, Taiwan, R.O.C.

Recommended Citation

Sun, Chien-Ting; Kwok, On-Lei Annie; Guan, Pai-Chen; and Shih, Wen-Kai (2018) "USING REPRODUCING KERNEL PARTICLE METHOD FOR SHALLOW WATER PROBLEMS," *Journal of Marine Science and Technology*: Vol. 26: Iss. 3, Article 14.
DOI: DOI: 10.6119/JMST.201806_26(3).0014
Available at: https://jmstt.ntou.edu.tw/journal/vol26/iss3/14

Journal of Marine Science and Technology, Vol. 26, No. 3, pp. 431-440 (2018)
DOI: 10.6119/JMST.2018.06_(3).0014

USING REPRODUCING KERNEL PARTICLE METHOD FOR SHALLOW WATER PROBLEMS

Chien-Ting Sun[1], On-Lei Annie Kwok[3], Pai-Chen Guan[2, 4], and Wen-Kai Shih[2]

Key words: shallow water equations, meshfree method, reproducing kernel particle method, high order approximation.

ABSTRACT

In this paper, a meshfree numerical scheme, which is based on the reproducing kernel particle method (RKPM), is proposed to solve the shallow water equations (SWEs). By applying the split coefficient matrix method on SWEs, RK approximation with upstream scheme can be employed for spatial discretization. Temporal discretization of SWEs is handled by the second-order total-variation diminishing Runge-Kutta method. The merits of the present method are verified by performing three numerical experiments, which are problems related to open channel flow, oblique hydraulic jump and two-dimensional dam break. It is found that the proposed meshfree numerical scheme is able to efficiently model the shallow water problems with high convergence rate and accuracy. When non-uniform discretization is used in conjunction with the proposed method, the order of approximation and accuracy can still be maintained.

I. INTRODUCTION

Shallow water equations (SWEs) are a set of hyperbolic first-order nonlinear partial differential equations. The SWEs are often applied for the simulation of large-scale hydraulic problems like river flow, tidal flow, and waves in the coastal region or inland area. For these free surface flows, the effects in the gravity direction compared to those in the other two directions are very small. Therefore, instead of solving the three-dimensional Navier-Stokes equations, the SWEs, which are obtained by integrating the Navier-Stokes equations over the flow depth, are suitable for these problems.

Many numerical methods had been utilized to solve the shallow-water problems. For example, finite difference method (FDM) has been applied to perform hydraulic simulations (Fennema and Chaudhry, 1990; Xing and Shu, 2005). Significant development has been focused on utilizing finite volume method (FVM) to simulate complex unsteady flow phenomena (Yoon and Kang, 2004; Xing and Shu, 2011). Finite element method is also widely used to solve SWEs (Liang et al., 2008; Young, 1991). However, the aforementioned mesh-based methods have a common difficulty of constructing a mesh and establishing the node-to-node connectivity, especially for problems with complex geometries. Moreover, their performance depends significantly on the quality of the mesh.

In the last few decades, meshfree methods, such as the smooth particle hydrodynamics (SPH) methods (Lucy, 1977; Gingold and Monaghan, 1977), diffuse element methods (Nayroles et al., 1992), element-free Galerkin methods (Belytschko et al., 1994) and the reproducing particle kernel method (RKPM), (Liu et al., 1995; Chen et al., 1996), had been developed extensively and used in a wide range of engineering applications. These meshfree methods do not require any mesh-generation and can achieve high order of approximation. In recent years, RKPM method has been advanced such that they can obtain solutions more efficiently and be applied on more complex problems. For instance, Wang and Chen (2014) developed a quasi-convex RK approximation scheme which can eliminate most of the negative regions of the high-order RK shape functions. This scheme is proven to be beneficial for vibration problems. Yreux and Chen (2016) developed a quasi-linear RK approximation scheme to correct the approximation error which is present near a boundary, crack or in regions with non-uniform discretization. Sun et al. (2018) developed a local re-construction of RK shape function to eliminate the numerical oscillation when using the high-order approximation for shock wave propagation problem.

Meshfree methods had also been applied to solve hydraulic problems governed by SWEs, for instance, SPH method (Ata and Soulaïmani, 2005; Vacondio et al., 2013) finite point method (Buachart et al., 2014), radial-basis-function (RBF) collocation method (Chou et al., 2015), natural element method (Du, 2000; Darbani et al., 2011), and element-free Galerkin methods (Du, 2000).

This paper is organized as follows: Section II introduces the basic theoretical formulation of RKPM and governing equations for the shallow water problems. Numerical treatment, includ-

Paper submitted 02/09/18; revised 05/07/18; accepted 05/29/18. Author for correspondence: Pai-Chen Guan (e-mail: paichen@ntou.edu.tw).
[1] *CR Classification Society.*
[2] *Department of Systems Engineering and Naval Architecture, National Taiwan Ocean University, Keelung, Taiwan, R.O.C.*
[3] *Department of Civil Engineering, National Taiwan University, Taipei, Taiwan, R.O.C.*
[4] *Center of Excellence for Ocean Engineering.*

ing upstream method, full transformation method and Runge-Kutta time integration method, are discussed in Section III. The performance of the proposed numerical method is demonstrated through three numerical examples in Section IV. Lastly, conclusions and discussions will be given based on the numerical results.

II. BASIC FORMULATIONS

1. Reproducing Kernel Approximation

Considering an arbitrary function $f(\mathbf{x})$, its numerical approximation $f^h(\mathbf{x})$ can be presented as (Chen et al., 1996):

$$f^h(\mathbf{x}) = \sum_I \Psi_a(\mathbf{x}; \mathbf{x}-\mathbf{x}_I)\tilde{f}_I \tag{1}$$

where Ψ_a is the RK shape function, and I represents the index for I^{th} particle. Therefore, $\tilde{f}_I$ and $\mathbf{x}_I$ are the nodal coefficient and position of the I^{th} particle respectively. The RK shape function can be written as:

$$\Psi_a = C(\mathbf{x}-\mathbf{x}_I)\phi_a(\mathbf{x}-\mathbf{x}_I) \tag{2}$$

where $C(\mathbf{x}-\mathbf{x}_I)$ and $\phi_a(\mathbf{x}-\mathbf{x}_I)$ are the correction function and kernel function, respectively. Index a refers to the value of the support size. In this paper, the B-spline function (Guan and Sun, 2014) is applied for the kernel function. The correction function is a polynomial function, which can be computed as:

$$C(\mathbf{x}-\mathbf{x}_I) = \mathbf{B}^T(\mathbf{x}-\mathbf{x}_I)\mathbf{M}^{-1}\mathbf{B}(0) \tag{3}$$

where

$$\mathbf{B}^T(\mathbf{x}-\mathbf{x}_I) = \begin{bmatrix} 1 & (x-x_I) & (y-y_I) \\ (x-x_I)^2 & (y-y_I)^2 & (x-x_I)(y-y_I) & \cdots \end{bmatrix} \tag{4}$$

$$\mathbf{M} = \sum_I \mathbf{B}(\mathbf{x}-\mathbf{x}_I)\mathbf{B}^T(\mathbf{x}-\mathbf{x}_I)\phi_a(\mathbf{x}-\mathbf{x}_I) \tag{5}$$

Substituting Eq. (3) into Eq. (2) yields the following RK shape function:

$$\Psi_a = \mathbf{B}^T(\mathbf{x}-\mathbf{x}_I)\mathbf{M}^{-1}\mathbf{B}(0)\phi_a(\mathbf{x}-\mathbf{x}_I) \tag{6}$$

The kernel function controls the continuity and smoothness of the RK approximation, and the support size determines the influence area of the RK particles. Therefore, a large support size means more neighboring particles would participate in the local approximation. Fig. 1 shows the first order RK shape function.

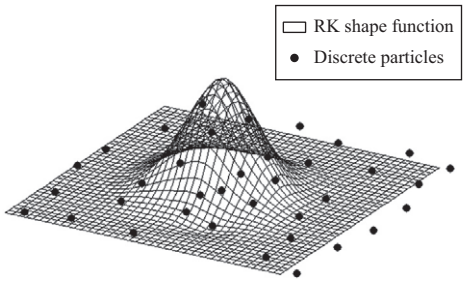

Fig. 1. The diagram of RK shape function.

2. Pseudo-Derivative of Reproducing Kernel Approximation

In this paper, we applied the pseudo-derivative (Krongauz and Belytschko, 1997) for the approximation of the derivative field. This method avoids calculating the derivative of every term in Eq. (6). Therefore, it can improve the efficiency during the process of building shape functions. To use pseudo-derivative, we assume that the derivative field can be presented as:

$$\partial f(\mathbf{x})/\partial \mathrm{x}^\alpha = \sum_I \tilde{\Psi}_I^\alpha \tilde{f}_I \tag{7}$$

where $\tilde{\Psi}^\alpha$ is the shape function of the derivative field and can be written as:

$$\tilde{\Psi}_I^\alpha = C^\alpha(\mathbf{x}-\mathbf{x}_I)\phi_a(\mathbf{x}-\mathbf{x}_I) \tag{8}$$

The indices $\alpha = 1, 2$ represent the two dimensions x, y respectively. The term x^α is the dimensions where the partial derivative is taken. Similar to the RK shape function, the shape function of the derivative field is given by:

$$\tilde{\Psi}_I^\alpha = \mathbf{B}^T(\mathbf{x}-\mathbf{x}_I)\mathbf{M}^{-1}\,\partial\mathbf{B}/\partial x^\alpha\,(0)\phi_a(\mathbf{x}-\mathbf{x}_I) \tag{9}$$

Fig. 2 shows the first-order pseudo derivative of the RK shape function.

3. SWEs

The SWEs can be derived from the Navier-Stokes equations by integrating them along the vertical (z) direction with the assumptions of negligible vertical acceleration and hydrostatic pressure distribution. The SWEs include the mass conservation equations:

$$\frac{\partial h}{\partial t} = -\left(\frac{\partial uh}{\partial x} + \frac{\partial vh}{\partial y}\right) \tag{10}$$

and the momentum conservation equations:

$$\begin{aligned} \frac{\partial u}{\partial t} + u\frac{\partial u}{\partial x} + v\frac{\partial u}{\partial y} + g\frac{\partial h}{\partial x} &= F_x \\ \frac{\partial v}{\partial t} + u\frac{\partial v}{\partial x} + v\frac{\partial v}{\partial y} + g\frac{\partial h}{\partial y} &= F_y \end{aligned} \tag{11}$$

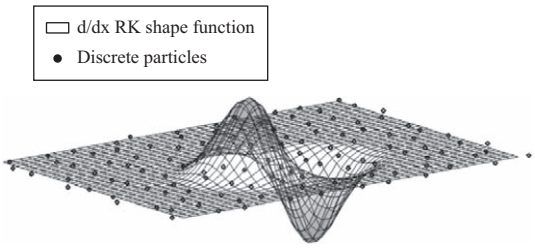

Fig. 2. The diagram of the first-order pseudo derivative of the RK shape function.

where h, u, and v are the water height, depth-averaged velocity in the x- and y-directions respectively. Under the assumption of incompressible fluid, the external forces F_x and F_y can be evaluated as:

$$\begin{aligned} F_x &= gSo_x - gSf_x + C_f v \\ F_y &= gSo_y - gSf_y + C_f u \end{aligned} \tag{12}$$

in which, g and C_f are the gravitational acceleration and the Coriolis coefficient, respectively. So is the seabed slope term, and S_f is the seabed friction term, which can be calculated as:

$$Sf_x = b^2 h^{-4/3} u\sqrt{u^2+v^2}\,;\; Sf_y = b^2 h^{-4/3} v\sqrt{u^2+v^2} \tag{13}$$

where b is the Manning's roughness coefficient. The SWEs in non-conservative form can be expressed as (Li and Fan, 2017):

$$\frac{\partial \mathbf{U}}{\partial t} + \mathbf{A}\frac{\partial \mathbf{U}}{\partial x} + \mathbf{B}\frac{\partial \mathbf{U}}{\partial y} = \mathbf{F} \tag{14}$$

where

$$\mathbf{U} = \begin{bmatrix} h \\ u \\ v \end{bmatrix};\; \mathbf{A} = \begin{bmatrix} u & h & 0 \\ g & u & 0 \\ 0 & 0 & u \end{bmatrix};\; \mathbf{B} = \begin{bmatrix} v & 0 & h \\ 0 & v & 0 \\ g & 0 & v \end{bmatrix};\; \mathbf{F} = \begin{bmatrix} 0 \\ F_x \\ F_y \end{bmatrix} \tag{15}$$

By applying Eq. (1) for the water depth and depth-averaged velocities, and using the pseudo-derivative shape function for the derivative field, the discrete form of SWEs would become:

$$\frac{\partial \mathbf{U}_I}{\partial t} = \mathbf{F}_I - \mathbf{A}_I \sum_J^{NP} \tilde{\Psi}^1_J \tilde{\mathbf{U}}_J - \mathbf{B}_I \sum_J^{NP} \tilde{\Psi}^2_J \tilde{\mathbf{U}}_J \tag{16}$$

where subscripts I, J represent the I^{th}, and J^{th} particles respectively, and NP is the total number of discrete RK particles that participate in the approximation of I^{th} particle. The $\tilde{\Psi}^{\alpha}$ is the pseudo-derivative of the RK shape function, and $\tilde{\mathbf{U}}_J$ is the so called "nodal coefficient vector" of the unknown field vector $\mathbf{U}$ at node J. We need to distinguish these two vectors ($\mathbf{U}$ and $\tilde{\mathbf{U}}$) in the formulation because the RK shape functions does not possess the Kronecker delta properties. The nodal coefficients of the RK approximation would deviate from the true values of the unknown field at the same node J when the support size increases. We will discuss how to make transformation between the real nodal values and the nodal coefficients in the next section.

III. NUMERICAL ALGORITHM

1. The RK Approximation with Upstream Scheme

In this paper, we use the split-coefficient matrix method (Fennema Robert and Chaudhry, 1990) to find the characteristics of the SWEs. With such characteristics, we would be able to employ the framework of upstream method and can simulate the propagation of waves in different directions.

Under the framework of split-coefficient matrix method, the coefficient matrices $\mathbf{A}$ and $\mathbf{B}$ from Eq. (14) are diagonalized in order to find the characteristic lines of the SWEs. The eigenvalues of matrix $\mathbf{A}$ are u, $u+c$, and $u-c$, where $c=\sqrt{gh}$. On the other hand, v, $v+c$, $v-c$ are the eigenvalues for matrix $\mathbf{B}$. Therefore, matrices $\mathbf{A}$ and $\mathbf{B}$ can be written as:

$$\mathbf{A}_I = \mathbf{P}^A_I \mathbf{D}^A_I \left(\mathbf{P}^A_I\right)^{-1};\; \mathbf{B}_I = \mathbf{P}^B_I \mathbf{D}^B_I \left(\mathbf{P}^B_I\right)^{-1} \tag{17}$$

where $\mathbf{P}$ is eigenvector matrix and $\mathbf{D}$ is a diagonal matrix containing the eigenvalues. The sign of the eigenvalues indicates the direction of the wave. Then according the wave direction, the eigenvalue matrix $\mathbf{D}$ can be further separated into $\mathbf{D}$+ and $\mathbf{D}$- as follows.:

$$\begin{aligned} \mathbf{A}^+_I &= \mathbf{P}_I \mathbf{D}^{A+}_I \mathbf{P}^A_I;\; \mathbf{A}^-_I = \mathbf{P}^A_I \mathbf{D}^{A-}_I \mathbf{P}^A_I; \\ \mathbf{B}^+_I &= \mathbf{P}^B_I \mathbf{D}^{B+}_I \mathbf{P}^B_I; \mathbf{B}^-_I = \mathbf{P}^B_I \mathbf{D}^{B-}_I \mathbf{P}^B_I; \end{aligned} \tag{18}$$

Substituting Eq. (18) into Eq. (16), the governing equation can be expressed as:

$$\begin{aligned} \frac{\partial \mathbf{U}_I}{\partial t} = \mathbf{F}_I &- \mathbf{A}^+_I \sum_J^{NP} \tilde{\Psi}^{1+}_J \tilde{\mathbf{U}}_J - \mathbf{A}^-_I \sum_J^{NP} \tilde{\Psi}^{1-}_J \tilde{\mathbf{U}}_J \\ &- \mathbf{B}^+_I \sum_J^{NP} \tilde{\Psi}^{2+}_J \tilde{\mathbf{U}}_J - \mathbf{B}^-_I \sum_J^{NP} \tilde{\Psi}^{2-}_J \tilde{\mathbf{U}}_J \end{aligned} \tag{19}$$

where $\tilde{\Psi}^{\alpha\pm}$ is pseudo-derivative of the RK shape function in the positive (or negative) direction of the wave propagation for the α-direction. When we perform the RKPM approximation, we should adjust the support size separately for the upstream and downstream components. For wave propagation in the positive direction, only the upstream particles would participate in the approximation. Conversely, when wave propagates in the negative direction, only the downstream particles would be chosen to form the local approximation. Fig. 3 depicts the 1st deriva-

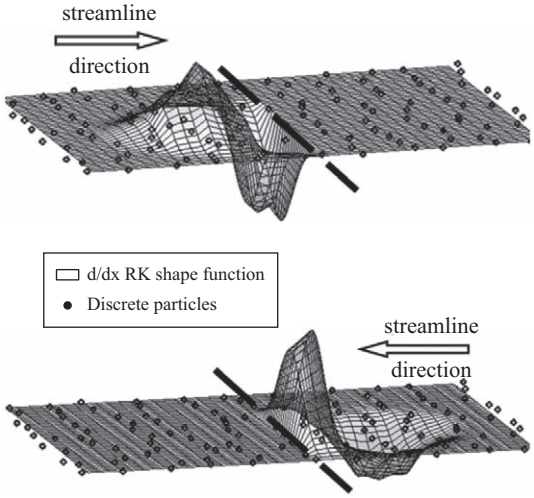

Fig. 3. First-order derivative of the shape function divided into positive and negative components along with the discrete particles.

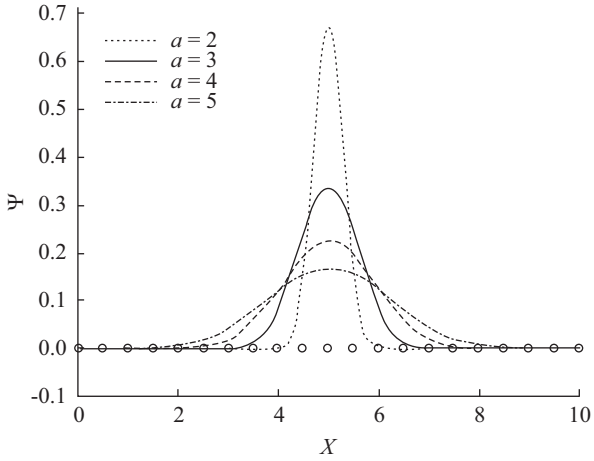

Fig. 4. The first-order RK shape function with different support sizes.

tive of the original shape function in both positive and negative directions, along with the RK discrete particles.

2. Full Transformation Method

In the RK approximation, when the support size increases, the shape function tends to be more "smooth", which is depicted in Fig. 4. This behavior would make the RK shape function lose the Kronecker delta property. Therefore, in Eq. (1), the nodal coefficients are not exactly equal to the real physical values at the particle location. In order to resolve this problem, the full transformation method is proposed to transform the nodal coefficient into physical value (Chen and Wang, 2000). The formulation is listed below:

$$\begin{bmatrix} \tilde{\mathbf{U}}_1 \\ \tilde{\mathbf{U}}_2 \\ \vdots \\ \tilde{\mathbf{U}}_{NP} \end{bmatrix} = \begin{bmatrix} \boldsymbol{\Phi}_{11} & \boldsymbol{\Phi}_{12} & \cdots & \boldsymbol{\Phi}_{1NP} \\ \boldsymbol{\Phi}_{21} & \boldsymbol{\Phi}_{22} & & \boldsymbol{\Phi}_{2NP} \\ \vdots & & \ddots & \vdots \\ \boldsymbol{\Phi}_{NP1} & \boldsymbol{\Phi}_{NP2} & \cdots & \boldsymbol{\Phi}_{NPNP} \end{bmatrix}^{-1} \begin{bmatrix} \mathbf{U}_1 \\ \mathbf{U}_2 \\ \vdots \\ \mathbf{U}_{NP} \end{bmatrix} \tag{20}$$

where

$$\boldsymbol{\Phi}_{IJ} = \left[\Psi_a(\mathbf{x}_\mathrm{I}; \mathbf{x}_\mathrm{I} - \mathbf{x}_\mathrm{J}) \quad \Psi_a(\mathbf{x}_\mathrm{I}; \mathbf{x}_\mathrm{I} - \mathbf{x}_\mathrm{J}) \quad \Psi_a(\mathbf{x}_\mathrm{I}; \mathbf{x}_\mathrm{I} - \mathbf{x}_\mathrm{J}) \right]^T \tag{21}$$

when all fields are approximated by the same set of RK shape functions. At every time step, in order to construct Eq. (19), we need to use Eq. (20) to recover the nodal coefficient vectors.

3. Time Integration

While second order RKPM spatial approximation is used in this study, second-order total-variation diminishing Runge-Kutta method (Gottlieb and Shu, 1996) is applied for the time integration. The time discretization of Eq. (16) can be written as:

$$\begin{aligned} \mathbf{U}_I^{n+1/2} &= \mathbf{U}_I^n + \Delta t \frac{\partial \mathbf{U}_I^n}{\partial t} \\ \mathbf{U}_I^{n+1} &= \frac{1}{2}\mathbf{U}_I^n + \frac{1}{2}\left(\mathbf{U}_I^{n+1/2} + \Delta t \frac{\partial \mathbf{U}_I^{n+1/2}}{\partial t} \right) \end{aligned} \tag{22}$$

in which, superscript n represents the n-th time step, and Δt is the time increment.

IV. NUMERICAL EXAMPLES

1. Open-Channel Flow Over a Hump

The first numerical example is the well-known benchmark problem for SWEs. In this example, the flow will pass through humps with two kinds of geometry. The basement of these two kinds of channel are frictionless The total length of the channel is 25 meters, and a unit width is applied as it is a one-dimensional problem.

The first basement geometry can be described by the following function (Liang et al., 2008):

$$Z_b = \begin{cases} 0.2 - 0.05(x-10)^2 & \text{if } 12 \ge x \ge 8 \\ 0 & \text{else} \end{cases} \tag{23}$$

The boundary conditions are water height (h) of 2 m at the downstream boundary, and a constant discharge q = 4.42 m^3/s at the upstream boundary. The initial conditions for the upstream boundary are specified as $\left[h \quad u \quad v \right]_0^T = \left[2 \quad 2.21 \quad 0 \right]^T$. The model of the basement and the steady-state solution of the water height are illustrated in Fig. 5.

In order to evaluate the convergence rate, 126, 251 and 501 RK particles with uniform discretization are used. Both first-order and second-order RK approximations are applied with a support size of $a = 5\Delta x$ and the same total number of particles,

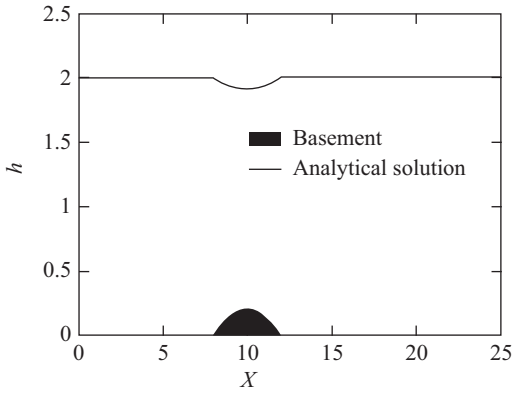

Fig. 5. The first type of basement and the steady-state open-channel flow.

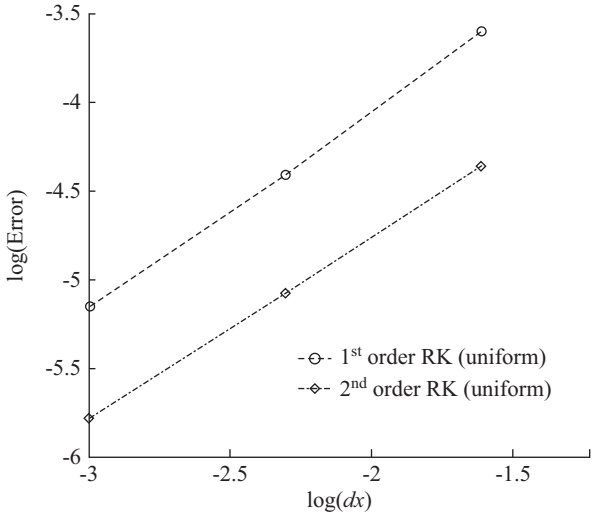

Fig. 6. The convergence test by first- and second-order RK approximation with 126, 251, and 501 particles with uniform discretization (for open channel flow over a semi-circular hump).

where Δx is the nodal distance used in the uniform discretization case. It should be noted that for all numerical examples presented in this paper, the same support size is used. A support size of $a = 5\Delta x$ is chosen because the latter numerical example with non-uniform discretization requires at least $a = 5\Delta x$ to achieve numerical stability. To make sure that the result would converge to the steady state solution, the total simulation time is set at $T = 400$ s with time step of $\Delta t = 0.005$. The estimation error for all one-dimensional problems is calculated by using the root-mean-square method, which is defined as:

$$e = \sqrt{\frac{1}{NP}\sum_{I}^{NP}\left(f - f^{h}\right)^{2}} \tag{24}$$

where f, f^h are exact and approximate solutions respectively. The convergence test results (for the solution of water height) obtained by using different orders of approximation are shown in Fig. 6.

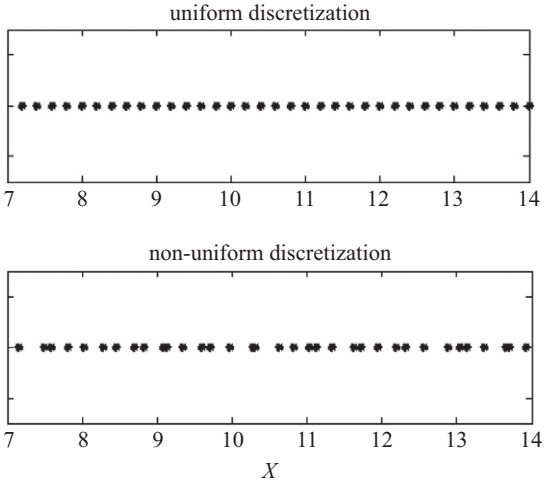

Fig. 7. The comparison of uniform and non-uniform discretization with 126 particles (for open channel flow over a semi-circular hump).

In Fig. 6, the rates of convergence by the first- and second-order approximations are 1.122 and 1.030 respectively. In this numerical example, the slope of the basement would create a discontinuous jump at the start and end points of the hump. However, the RK approximation is highly smooth and continuous. The rate of convergence is bounded when the RK approximation tries to simulate the discontinuous region, even though a high-order RK shape function is applied.

One of the many advantages of the meshfree method is that it can be easily applied with non-uniform discretization while the same accuracy is maintained. Here, we re-examine the open-channel flow problem (with the first basement geometry) with non-uniform discretization. The total number of discrete particles are 126, 251, and 501 which are the same as the uniform discretization case. The distance between particles has a random perturbation ε. The perturbation is set as $|\varepsilon| \le 0.4\Delta x$. The particle arrangement with non-uniform discretization (with 126 particles) is presented in Fig. 7.

Generally, for non-uniform discretization, the RK shape functions would have different sizes of influence domain for different particles. However, with the use of the full transformation method, a constant support size can be used conveniently while the same order of accuracy can be maintained. In this case, the support size is $a = 5\Delta x$ for both first- and second-order RK approximations. The errors in the simulated water-height from both uniform and non-uniform discretization cases (for different number of particles) are compared and shown in Fig. 8. It can be observed that the error in the simulation for the non-uniform discretization case does not monotonically increase with the "average" nodal distance. This is because the nodal distance is randomly assigned. If a large nodal distance is coincidentally used for the discontinuous region, a large error would likely be resulted.

For non-uniform discretization, a higher order approximation can yield better accuracy. In addition, it can achieve similar level

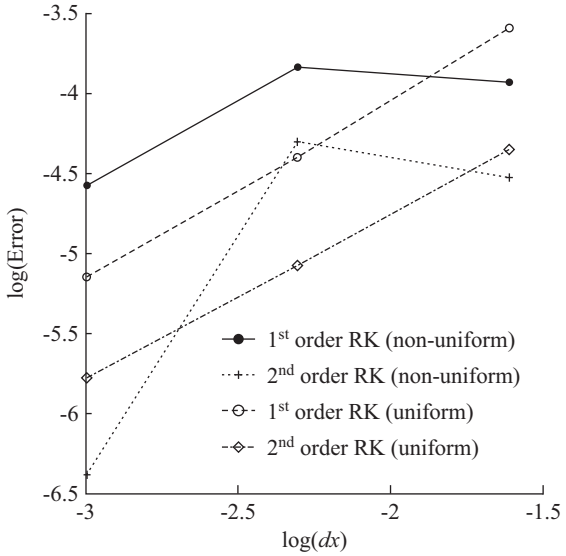

Fig. 8. The convergence test result of uniform and non-uniform discretization cases with first- and second-order RK approximations (for open channel flow over a semi-circular hump).

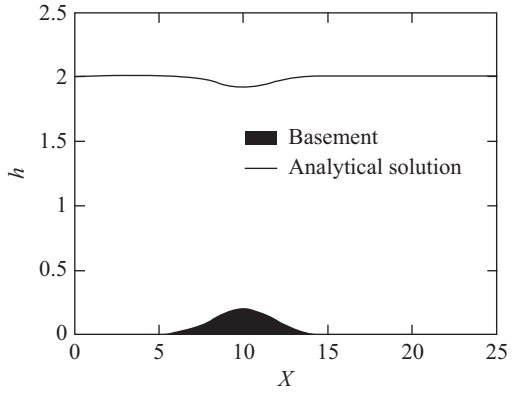

Fig. 9. The second type of basement and the steady-state open-channel flow.

of accuracy as the uniform discretization case. Therefore, the proposed method has the robust ability for using the non-uniform discretization.

For the open channel flow problem, a second geometry, which can be described by an exponential function (Chou et al., 2015), is used to describe the basement:

$$Z_b = 0.2e^{-0.16(x-10)^2} \tag{25}$$

The model of the channel and the analytical solution with the same boundary conditions are shown in Fig. 9.

The first-order and second-order RK approximations are applied with support size $a = 5\Delta x$. The error in the simulated water height is used as the measure for the convergence test. The rates of convergence for the first- and second-order approximation with 26, 51, 126, and 251 particles are compared and shown in Fig. 10.

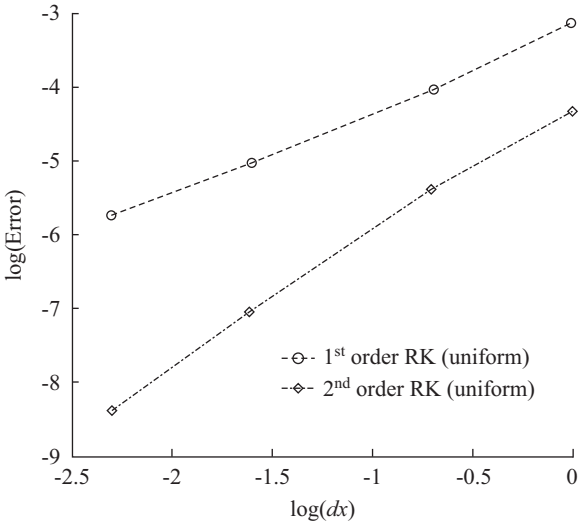

Fig. 10. The convergence test by first- and second-order RK approximation with 26, 51, 126, and 251 particles with uniform discretization (for open channel flow over a hump with exponential shape).

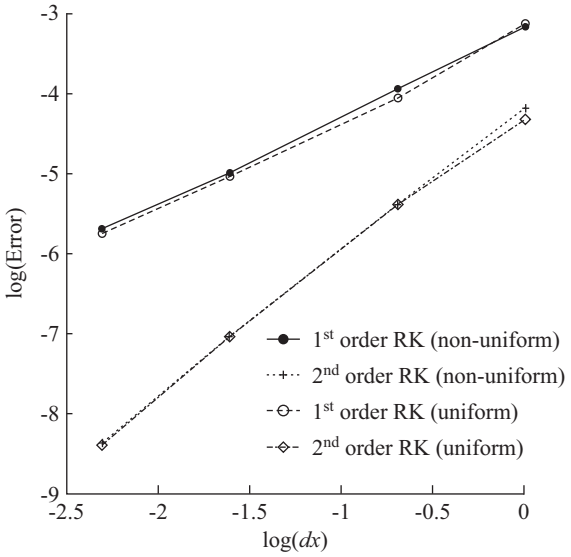

Fig. 11. The convergence test of uniform and non-uniform discretization by first- and second-order RK approximation (for open channel flow over a hump with exponential shape).

In Fig. 10, the rates of convergence obtained by using the first- and second RK approximations with uniform discretization are 1.04 and 1.87 respectively. Unlike the previous case (open-channel flow with a discontinuous semi-circular hump), the numerical results obtained by using higher order RK shape function can obtain better accuracy and higher rate of convergence. For the non-uniform discretization case, the perturbation of the distance between particles is also set as $|\varepsilon| \le 0.4\Delta x$. Convergence test results for the uniform and non-uniform discretization cases are compared and shown in Fig. 11. The simulations were performed by using first- and second-order RK approximations with 26, 51, 126, and 251 particles.

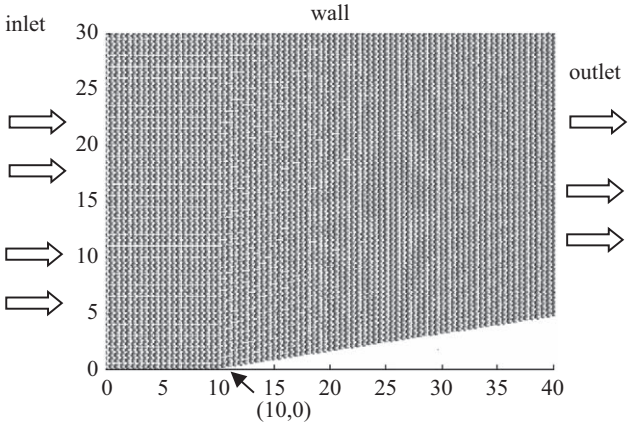

Fig. 12. The model for the oblique hydraulic jump.

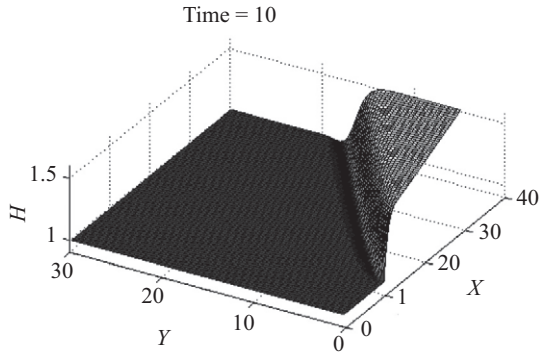

Fig. 13. The numerical result of oblique hydraulic jump problem at 10 second (when steady state is reached).

As shown in Fig. 11, when the geometry of the seabed is continuous, the convergence rate for the non-uniform discretization model is exactly the same as the rate for the uniform discretization model. In contrast, as shown in Fig. 8, the convergence rate for non-uniform discretization model (with discontinuous seabed) is highly dependent on the nodal arrangement around the discontinuous region.

2. Oblique Hydraulic Jump

This example is a well-known two-dimensional hydraulic problem. The open channel is 40 m long and has a width of 30 m. During the wave propagation, the flow would hit a converging wall with a deflection angle $\theta = 8.95°$. The flow would create a discontinuous shock, which develops from the initial point of the converging wall. The shock would exit the model with a shock angle $\beta = 30°$ (Buachart et al., 2014). The top and bottom parts of the channel are wall boundaries which are assumed to be flat and frictionless. The left and right sides are the inlet and outlet boundaries respectively. In this problem, the total number of discrete particles is 4860 with uniform distance $\Delta s = 0.5$ at the inlet boundary. The model of this problem including the domain discretization are presented in Fig. 12.

For this flow channel, the initial conditions of the water height and velocities in both directions are $h = 1$ m, $u = 8.75$ m/s, v = 0 respectively. The convergence criterion for achieving the steady state is defined by the L2 error norm:

$$e = \sqrt{\sum_I \left(h_I^{n+1} - h_I^n \right)^2} \tag{26}$$

When $e < 10^{-5}$, the simulation is considered to have reached steady state. The simulation of the water jump at steady state is shown in Fig. 13. In Fig. 13, we can observe that the water-stack phenomenon which is due to the contraction of the channel.

In order to test the convergence of the proposed method, we apply 1230, and 4860 particles respectively in the numerical simulation of the oblique hydraulic jump problem. The exact and numerical solutions, in terms of water-height contour diagrams, are presented in Fig. 14.

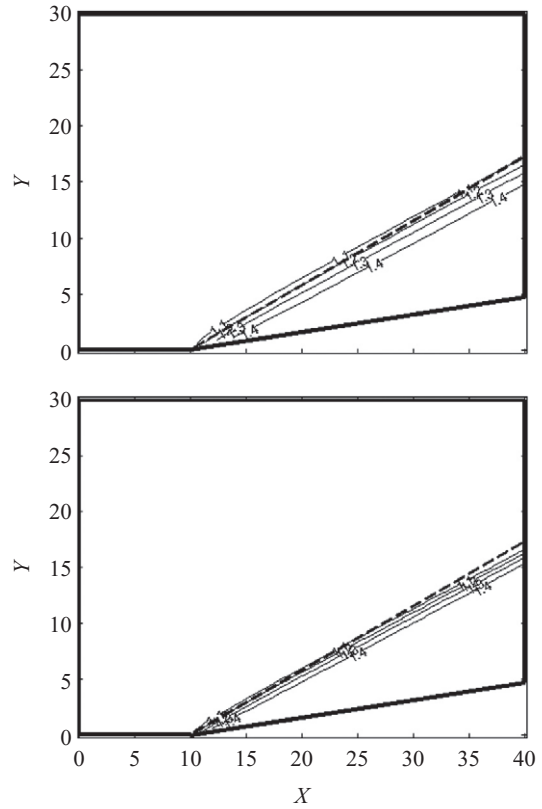

Fig. 14. The comparison of contour lines of water height by 1230 (top figure), and 4860 particles (bottom figure) , where the dash line is the exact shock front

As shown in Fig. 14, the proposed method can well describe the water stack phenomenon. By increasing the number of particles, better accuracy can be achieved. Therefore, the proposed method has robustness and reliability for simulating two dimensional flow problem.

3. Two Dimensional Dam-Break Problem

In this problem, the computational domain is a square tank with 200 m for each side. There is a dam located in the middle

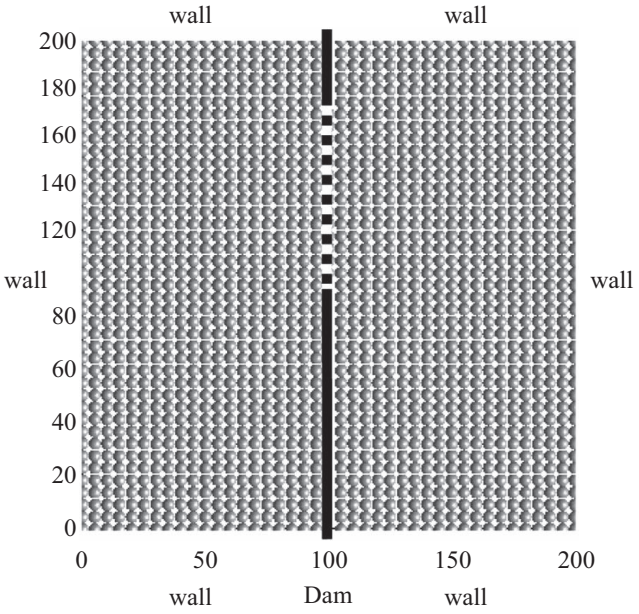

Fig. 15. The model of the dam-break problem with 1546 discrete particles.

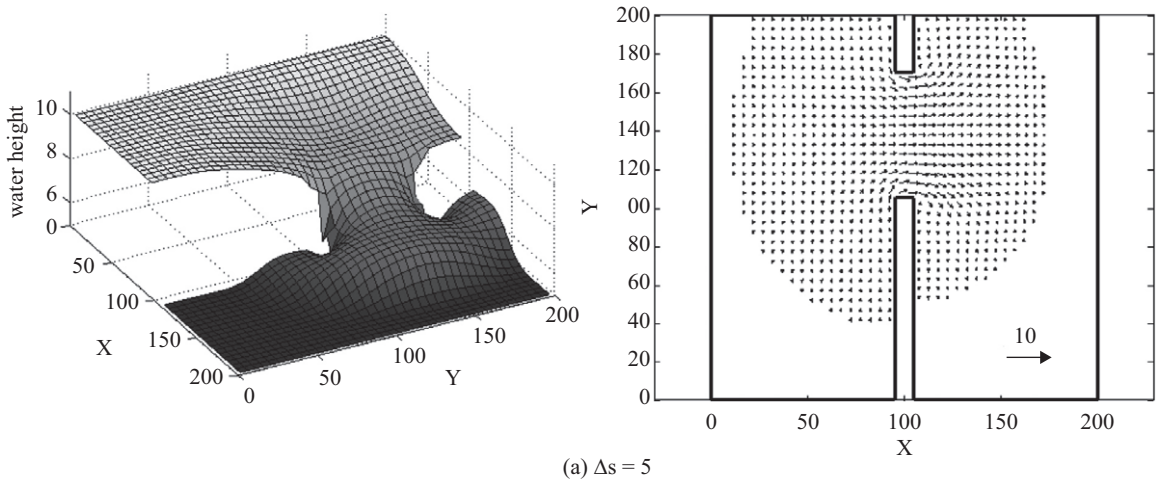

(a) Δs = 5

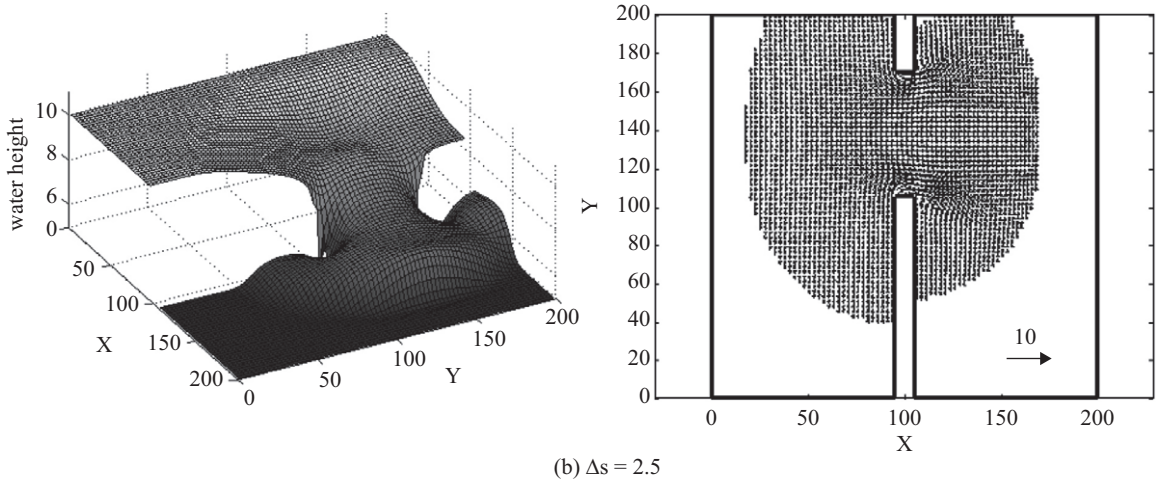

(b) Δs = 2.5

Fig. 16. Numerical results of water height and velocity field of dam-break problem at t = 7.2 s.

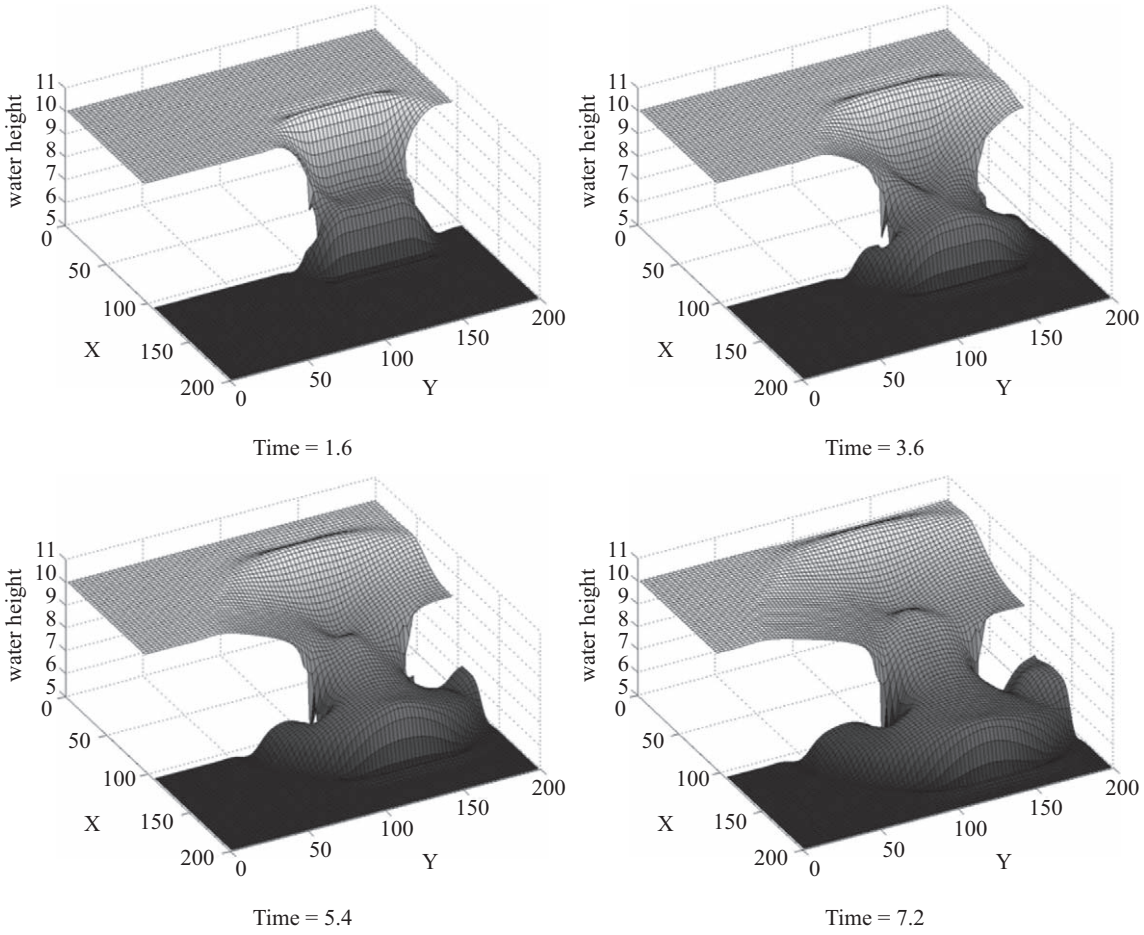

Fig. 17. The water surface profile at 1.6, 3.5, 5.4, and 7.2 second for the dam-break problem.

of the tank, and the size of the dam is 200 m in length and 10 m in width. The four side boundaries of the tank are all walls with free slip condition, and the bottom of the tank is frictionless. The model of this problem is shown in Fig. 15.

The left side is the catchment area. The water height on the left side is 10 m. and the water height in the downstream is 5 m. The dam has a non-symmetric breach from y =105 m to 170 m. The dam would rapidly break during the initial state, which would create a positive shock wave that propagates towards downstream and a negative fan wave that propagates towards upstream. In this problem, the second order RK approximation is applied with support size $a = 2.5\Delta s$, where Δs is the distance between particles. The total simulation time is 7.2 seconds to avoid the wave from hitting the left and right boundaries.

Fig. 16 shows the numerical results in terms of water height and velocity field by using $\Delta s = 5$ and $\Delta s = 2.5$ at 7.2 second. The numerical results are compared to the solutions by (Sun et al., 2013; Chou et al., 2015; Li and Fan, 2017). The water surface profiles at different instants are presented in Fig. 17. Both upstream and downstream waves can be well described, suggesting that the proposed method are stable and reliable for two dimensional dam-break problems.

V. CONCLUSION

In this study, meshfree reproducing kernel particle method is applied in conjunction with the upstream scheme and second-order Runge-Kutta time integration scheme to model several open channel flow and dam break problems. Through the numerical simulations, the proposed model was demonstrated to achieve accuracy with high convergence rate. Moreover, model with non-uniform discretization was successfully implemented with the proposed meshfree method and found to be very efficient even though discontinuity was expected in the solution field. The ease of using non-uniform discretization would hence be a key advantage of the proposed method over other numerical schemes.

REFERENCES

Ata, R., and A. Soulaïmani (2005). A stabilized SPH method for inviscid shallow water flows, International Journal for Numerical Methods in Fluids 47. 139-59.

Belytschko, T., Y. Y. Lu and L. Gu (1994). Element-free Galerkin methods, International Journal for Numerical Methods in Engineering 37. 229-56.

Buachart, C., W. Kanok-Nukulchai, E. Ortega and E. Onate (2014). A Shallow Water Model by Finite Point Method, International Journal of Computa-

tional Methods 11. 1350047.
Chen, J. S., C. H. Pan, C. T. Wu and W. K. Liu (1996). Reproducing kernel particle methods for large deformation analysis of non-linear structures, Computer Methods in Applied Mechanics and Engineering 139. 195-227.
Chen, J. S. and H. P. Wang (2000). New boundary condition treatments in meshfree computation of contact problems, Computer Methods in Applied Mechanics and Engineering 187. 441-68.
Chou, C. K., C. P. Sun, D. L. Young, J. Sladek and V. Sladek (2015). Extrapolated local radial basis function collocation method for shallow water problems, Engineering Analysis with Boundary Elements 50. 275-90.
Darbani, M., A. Ouahsine, P. Villon, H. Naceur and H. Smaoui (2011). Meshless method for shallow water equations with free surface flow, Applied Mathematics and Computation 217. 5113-24.
Du, C. (2000). An element-free Galerkin method for simulation of stationary two-dimensional shallow water flows in rivers, Computer Methods in Applied Mechanics and Engineering 182. 89-107.
Fennema, R., J. and M. H. Chaudhry (1990). Explicit Methods for 2-D Transient Free Surface Flows, Journal of Hydraulic Engineering 116. 1013-34.
Gingold, R. A. and J. J. Monaghan (1977). Smoothed particle hydrodynamics - Theory and application to non-spherical stars, Monthly Notices of the Royal Astronomical Society 181. 375-89.
Gottlieb, S., and C.-W. Shu. 1996. *Total Variation Diminishing Runge-Kutta Schemes*.
Guan, P.-C. and C.-T. Sun (2014). The Isoparametric Reproducing Kernel Particle Method for nonlinear deformation of plates, Engineering Analysis with Boundary Elements 42. 67-76.
Krongauz, Y. and T. Belytschko (1997). Consistent pseudo-derivatives in meshless methods, Computer Methods in Applied Mechanics and Engineering 146. 371-86.
Li, P.-W. and C.-M. Fan (2017). Generalized finite difference method for two-dimensional shallow water equations, Engineering Analysis with Boundary Elements 80. 58-71.
Liang, S.-J., J.-H. Tang and M.-S. Wu (2008). Solution of shallow-water equations using least-squares finite-element method, Acta Mechanica Sinica 24. 523-32.
Liu, W. K., S. Jun and Y. F. Zhang (1995). REPRODUCING KERNEL PARTICLE METHODS, International Journal for Numerical Methods in Fluids 20. 1081-106.
Lucy, L. B. (1977). A numerical approach to the testing of the fission hypothesis, The Astronomical Journal 82. 1013.
Nayroles, B., G. Touzot and P. Villon (1992). Generalizing the finite element method: Diffuse approximation and diffuse elements, Computational Mechanics 10. 307-18.
Sun, C. P., D. L. Young, L. H. Shen, T. F. Chen and C. C. Hsian (2013). Application of localized meshless methods to 2D shallow water equation problems, Engineering Analysis with Boundary Elements 37. 1339-50.
Sun, C. T., P. C. Guan, J. H. Jiang and O. L. A. Kwok (2018). The weighted reconstruction of reproducing kernel particle method for one-dimensional shock wave problems, Ocean Engineering 149. 325-40.
Vacondio, R., B. D. Rogers, P. K. Stansby and P. Mignosa (2013). A correction for balancing discontinuous bed slopes in two-dimensional smoothed particle hydrodynamics shallow water modeling, International Journal for Numerical Methods in Fluids 71. 850-72.
Wang, D. and P. Chen (2014). Quasi-convex reproducing kernel meshfree method, Computational Mechanics 54. 689-709.
Xing, Y. and C.-W. Shu (2005). High order finite difference WENO schemes with the exact conservation property for the shallow water equations, Journal of Computational Physics 208. 206-27.
Xing, Y. and C.-W. Shu (2011). High-order finite volume WENO schemes for the shallow water equations with dry states, Advances in Water Resources 34. 1026-38.
Yoon T., H. and S.-K. Kang (2004). Finite Volume Model for Two-Dimensional Shallow Water Flows on Unstructured Grids, Journal of Hydraulic Engineering 130. 678-88.
Young, D. L. (1991). Finite element modeling of shallow water wave equations, Journal of the Chinese Institute of Engineers 14. 143-55.
Yreux, E. and J. S. Chen (2016). A quasi-linear reproducing kernel particle method, International Journal for Numerical Methods in Engineering 109. 1045-64.